Smart Mater. Struct. **19** (2010) 055009 (8pp) doi:10.1088/0964-1726/19/5/055009

# A dynamic model for a displacement amplified magnetostrictive driver for active mounts

**Suryarghya Chakrabarti and Marcelo J Dapino**

Department of Mechanical Engineering, Ohio State University, Columbus, OH 43210, USA

E-mail: chakrabarti.3@osu.edu and dapino.1@osu.edu

Received 11 November 2009, in final form 17 January 2010
Published 31 March 2010
Online at stacks.iop.org/SMS/19/055009

**Abstract**

A magnetostrictive actuator with a hydraulic displacement amplification mechanism is designed to be used as a driver in active engine mounts. The dynamic response of the actuator is quantified in terms of the output displacement and the magnetostriction. Eddy current losses are modeled as a one-dimensional magnetic diffusion problem in cylindrical coordinates. The Jiles–Atherton model is used to describe the magnetization state of the material as a function of applied magnetic fields. Magnetostriction, which is modeled as a single-valued function of magnetization, provides an input to the mechanical model describing the system vibrations. Friction at the elastomeric seals is modeled using the LuGre (Lund–Grenoble) friction model for lubricated contacts. Results show that the model accurately describes the dynamic behavior of the actuator up to 500 Hz. An order analysis of the data and calculated responses shows that the model describes the fundamental and higher-order spectral components generated by the device.

(Some figures in this article are in colour only in the electronic version)

## 1. Introduction

An engine mount is used to isolate engine vibrations from the passenger compartment and prevent excessive engine bounce from shock excitations. An active mount consists of a passive hydro-mount combined with an actuator which modulates the pressure of the hydraulic fluid so as to reduce the mount's force transmissibility. Thus the performance of an active mount depends heavily on the performance of the actuator. Many electromagnetic actuators [1–3] have been suggested which improve the vibration isolation characteristics of active mounts. However, these actuators exhibit a frequency bandwidth lower than 80 Hz. To achieve broader frequency bandwidth, actuators using smart material drivers have been considered [4–6].

The smart materials capable of producing broadband response have a small stroke. Hence their utilization in active mounts requires a stroke amplification mechanism. Hydraulic amplification [7–9] is particularly attractive as a means to achieve large mechanical gains in a restricted space. However, in most of the existing designs the mechanical performance is significantly degraded by internal friction and compliances in the fluid chamber components. Linear models fail to account for these effects, which carry intrinsic nonlinearities and hysteresis. Advanced modeling is therefore required to accurately describe and analyze the behavior of hydraulically amplified actuators.

In this paper we present a dynamic model for the coupled response of a hydraulically amplified magnetostrictive actuator for active mounts considering losses due to internal friction and fluid chamber compliance. The primary use of the proposed model is device design and control. The model is developed to describe the dynamic response of the hydraulically amplified Terfenol-D actuator developed by Chakrabarti and Dapino [10]. The response of the magnetostrictive material is modeled with a nonlinear and hysteretic formulation for magnetization as a function of applied fields and bias stress. The Jiles–Atherton model is coupled with Maxwell's equations in order to quantify the radial dependence of magnetization and associated dynamic losses. Magnetostriction, which is modeled as a single-valued function of magnetization, provides an input to the mechanical model. Friction at the elastomeric seals is described with the LuGre dynamic friction model. The resulting formulation thus incorporates friction phenomena such as stick-slip, pre-sliding displacement and the Stribeck effect. Structural dynamics of

 

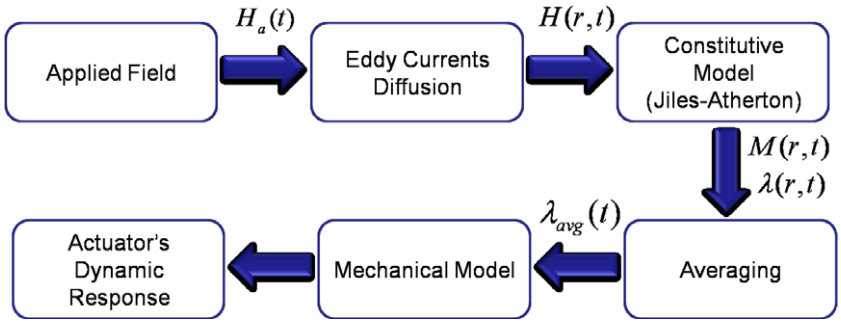


**Figure 1.** Flowchart for the actuator model.

the support is considered in order to increase the accuracy of the mechanical model.

### *1.1. Model structure*

Modeling the strain–field hysteresis loops for magnetostrictive materials has been a traditionally difficult problem. Numerous models exist which describe the strain–field loops at quasi-static frequencies. Modeling the dynamic strain–field relationship in magnetostrictive transducers is even more challenging because of dynamic magnetic losses and magnetoelastic coupling induced by vibration of structural components.

An approach to model the strain–field loops was developed by Sarawate and Dapino [11] where the radial dependence of field in a magnetostrictive rod is established by solving the magnetic diffusion equation. A similar modeling approach is followed in this paper (figure 1). The principal difference lies in the way the averaging of the field is done and the complexity of the loading on the magnetostrictive rod. In [11] an average effective field is obtained by formulating a weighted sum of the field at different radii while in the current work the Jiles Atherton model with input $H(r,t)$ is used to calculate the magnetization $M(r,t)$. The magnetostriction $\lambda(r,t)$ is directly calculated from $M(r,t)$. Subsequent averaging yields an average magnetostriction ($\lambda_{\text{avg}}$). The dynamic strain of the driver is obtained by coupling the magnetization model with the mechanical model.

In [11] the mechanical load acting on the driver is a single degree-of-freedom linear spring, mass, and damper system which allows to resolve the magnetostriction waveform into Fourier components. The response of the mechanical system to those components is calculated in the frequency domain. In the present work, the mechanical system consists of a hydraulic amplification mechanism with compliances and frictional losses at the seals. Due to the nonlinear nature of this system, the entire model is solved numerically in the time domain and the Fourier components of the Terfenol-D strain and total actuator displacement are calculated. Another important difference is the range of fields used to excite the Terfenol-D driver. In [11] the rod is driven at relatively lower fields (16 kA $\text{m}^{-1}$ pk–pk). This results in reduced nonlinearity in the material response. Here the applied field is $\approx 55$ kA $\text{m}^{-1}$ which gives rise to increased nonlinearity and hysteresis in the response.

## 2. Magnetic-field diffusion

Dynamic losses due to eddy currents can be quantified through Maxwell's equations,

$$\nabla \times H = J + \frac{\partial D}{\partial t}, \tag{1}$$

$$\nabla \times E = \frac{\partial B}{\partial t}. \tag{2}$$

Here, $H$ and $E$ respectively denote magnetic and electric fields; $J$ is the current density ($J = \sigma E$ for ohmic materials), and $\sigma$ is the constant electrical conductivity of the medium. The second term on the right hand side of (1) is known as displacement current and gives rise to electromagnetic radiation. This term can be neglected for the frequency range in which magnetostrictive transducers are operated. Further, assuming the change in magnetic flux density $B$ to be independent of the change in stress on the material, the spatial variation of magnetic field can be obtained by combining (1) and (2),

$$\begin{aligned} \nabla \times \nabla \times H &= \nabla \times J \\ &= \nabla \times (\sigma E) \\ &= -\sigma \left( \frac{\partial B}{\partial t} \right) \\ &= -\sigma \mu \left( \frac{\partial H}{\partial t} \right), \end{aligned} \tag{3}$$

where $\mu$ is the magnetic permeability of the material. The left hand side of (3) can be expressed as

$$\begin{aligned} \nabla \times \nabla \times H &= \nabla (\nabla \cdot H) - \nabla^2 H \\ &= \nabla \left( \nabla \cdot B \frac{1}{\mu} \right) - \nabla^2 H \\ &= -\nabla^2 H \; (\because \nabla \cdot B = 0). \end{aligned} \tag{4}$$

For cylindrical geometries, (3) and (4) give a magnetic diffusion equation of the form

$$\frac{\partial^2 H}{\partial r^2} + \frac{1}{r} \frac{\partial H}{\partial r} = \sigma \mu \frac{\partial H}{\partial t}. \tag{5}$$

The boundary condition at the surface of the rod for a harmonically applied field is $H(R,t) = H_0 e^{i\omega t}$. We assume the solution to be of the form $H_0 \tilde{h}(r) e^{i\omega t}$ where $\tilde{h}(r)$ is a

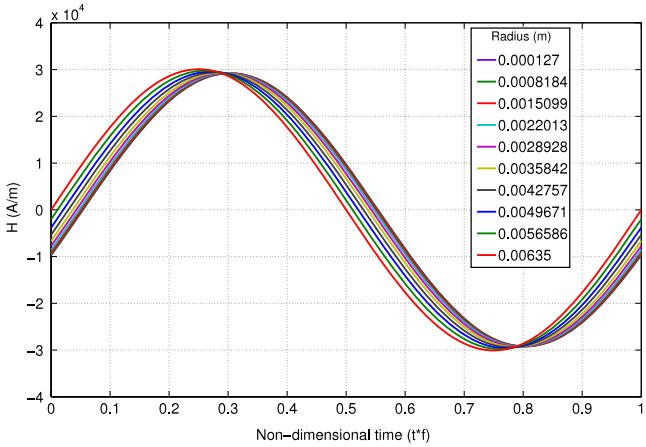


**Figure 2.** Field at 10 discrete radii from $r = 0.127$ to 6.35 mm.

complex function of the radius $r$. Equation (5) then reduces to

$$\frac{\partial^2 \tilde{h}}{\partial r^2} + \frac{1}{r}\frac{\partial \tilde{h}}{\partial r} - \mathrm{i}\sigma\mu\omega\tilde{h} = 0. \tag{6}$$

Assuming $\mu$ to be constant over the range of applied fields, the solution to (6) can be written as done in [12],

$$\tilde{h}(r) = \frac{I_0(q(r))}{I_0(q(R))}, \tag{7}$$

where $I_0$ is the modified Bessel function of order zero, $q(r) = (\sqrt{\mathrm{i}\sigma\mu\omega})r$ and $R$ is the radius of the magnetostrictive rod. Figure 2 shows the radial dependence of magnetic field in the rod at 500 Hz for $\mu = 5\mu_0$ and $1/\sigma = 58 \times 10^{-8}\ \Omega$ m. The magnetic field decreases toward the center of the rod and lags behind the field at the periphery of the rod.

## 3. Jiles–Atherton equations

The Jiles–Atherton model is used to describe the magnetization of the magnetostrictive material as a function of the applied magnetic field. The basic governing equations of the model are described here. For a detailed derivation of the equations the reader is pointed to [13]. The total magnetization at any instant of time can be written as a combination of an anhysteretic and an irreversible component,

$$M = cM_{\mathrm{an}} + (1-c)M_{\mathrm{irr}}, \tag{8}$$

in which $c$ is a reversibility parameter that accounts for reversible bowing of domain walls. When $c = 1$, domain wall motion is completely reversible and when $c = 0$, domain wall motion is completely irreversible. The anhysteretic magnetization is given by the Langevin function as

$$M_{\mathrm{an}} = M_{\mathrm{s}}\left(\coth\left(\frac{H_{\mathrm{e}}}{a}\right) - \left(\frac{a}{H_{\mathrm{e}}}\right)\right), \tag{9}$$

where $a$ is a shape parameter that controls the slope of the anhysteretic magnetization curve, $M_{\mathrm{s}}$ is the saturation magnetization of the material, and $H_{\mathrm{e}}$ is an effective field given by [14]

$$H_{\mathrm{e}} = H + \underbrace{\left(\alpha + \frac{9}{2}\frac{\sigma_{\mathrm{bias}}\lambda_{\mathrm{s}}}{\mu_0 M_{\mathrm{s}}^2}\right)}_{\tilde{\alpha}} M. \tag{10}$$

Here, $\sigma_{\mathrm{bias}}$ is the applied bias stress acting on the rod, $\alpha$ is a parameter that quantifies magnetic domain interactions and $\lambda_{\mathrm{s}}$ is saturation magnetostriction. The derivative of the total magnetization with respect to the applied field can be written as

$$\begin{aligned}\frac{\mathrm{d}M}{\mathrm{d}H} &= c\frac{\mathrm{d}M_{\mathrm{an}}}{\mathrm{d}H} + (1-c)\frac{\mathrm{d}M_{\mathrm{irr}}}{\mathrm{d}H} \\ &= c\frac{\mathrm{d}M_{\mathrm{an}}}{\mathrm{d}H_{\mathrm{e}}}\left(\frac{\mathrm{d}H_{\mathrm{e}}}{\mathrm{d}H}\right) + (1-c)\frac{\mathrm{d}M_{\mathrm{irr}}}{\mathrm{d}H_{\mathrm{e}}}\left(\frac{\mathrm{d}H_{\mathrm{e}}}{\mathrm{d}H}\right),\end{aligned} \tag{11}$$

where

$$\frac{\mathrm{d}H_{\mathrm{e}}}{\mathrm{d}H} = 1 + \tilde{\alpha}\frac{\mathrm{d}M}{\mathrm{d}H}. \tag{12}$$

The irreversible magnetization is calculated through a law of approach to the anhysteretic magnetization,

$$\frac{\mathrm{d}M_{\mathrm{irr}}}{\mathrm{d}H_{\mathrm{e}}} = \frac{M_{\mathrm{an}} - M_{\mathrm{irr}}}{\delta k}, \tag{13}$$

where $k$ is a parameter that quantifies the energy required to break pinning sites and $\delta$ has a value of $+1$ for increasing fields and $-1$ for decreasing fields. The derivative of the anhysteretic magnetization relative to the effective field is

$$\frac{\mathrm{d}M_{\mathrm{an}}}{\mathrm{d}H_{\mathrm{e}}} = \frac{M_{\mathrm{s}}}{a}\left(-\left(\frac{1}{\sinh\left(\frac{H_{\mathrm{e}}}{a}\right)}\right)^2 + \left(\frac{a}{H_{\mathrm{e}}}\right)^2\right), \tag{14}$$

Recognizing that the field is radially dependent, combination of (11)–(14) yields a single expression for the variation of $M(r)$ with respect to $H(r)$,

$$\frac{\mathrm{d}M}{\mathrm{d}H}(r) = \underbrace{\left[c\frac{\mathrm{d}M_{\mathrm{an}}}{\mathrm{d}H_{\mathrm{e}}}(r) + \frac{M_{\mathrm{an}}(r) - M(r)}{\delta(r)k}\right]}_{\Phi_{(M(r))}}\left[1 + \tilde{\alpha}\frac{\mathrm{d}M}{\mathrm{d}H}(r)\right], \tag{15}$$

which can be rearranged to give

$$\frac{\mathrm{d}M}{\mathrm{d}H}(r) = \left(\frac{\Phi_{(M(r))}}{1 - \tilde{\alpha}\Phi_{(M(r))}}\right). \tag{16}$$

Assuming the prestress is sufficiently large, magnetostriction can be approximately modeled as a single-valued function of magnetization through the relation

$$\lambda(r) = \frac{3}{2}\frac{\lambda_{\mathrm{s}}}{M_{\mathrm{s}}^2}M(r)^2. \tag{17}$$

An average magnetostriction can then be obtained by conducting a weighted sum over the cross-section of the rod,

$$\lambda_{\mathrm{avg}} = \frac{1}{\sum_{i=1}^{n} N(r_i)}\sum_{i=1}^{n}\lambda(r_i)N(r_i), \tag{18}$$

where $r_i$ are the discrete radii at which the magnetostriction is evaluated and $N(r_i)$ are the weights which are proportional to $r_i$. Figure 3 shows how the average magnetostriction decreases and becomes delayed with increasing actuation frequency.

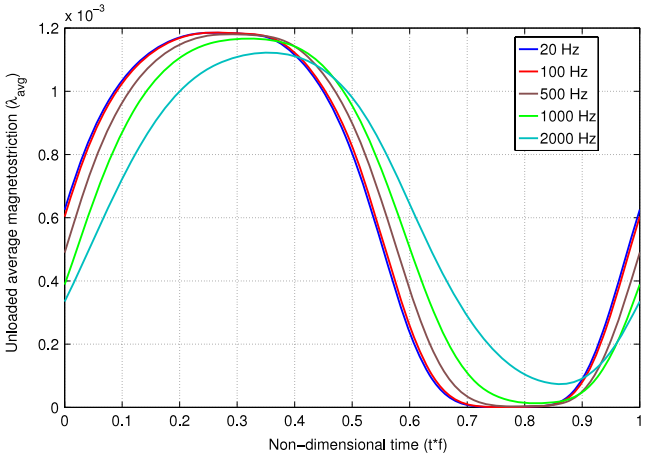


**Figure 3.** $\lambda_{avg}$ at different frequencies.

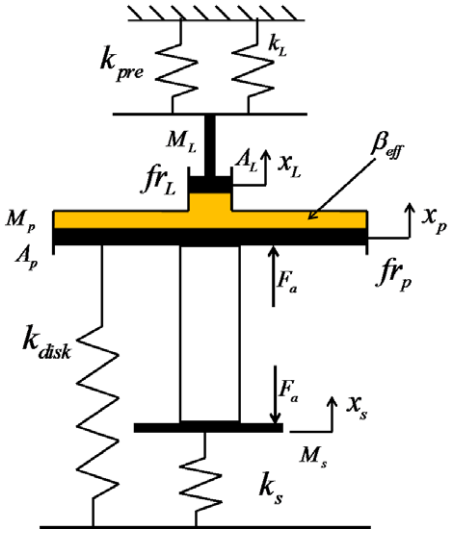


**Figure 4.** Mechanical model for the magnetostrictive mount actuator considered in this study.

## 4. Mechanical model

A mechanical model for the actuator is shown in figure 4. The pressure variation in the fluid can be linearized for small volumetric changes as follows

$$\Delta p = \beta \frac{\Delta V}{V_{\text{ref}}}, \tag{19}$$

where $\beta$ is the fluid's bulk modulus and $V_{\text{ref}}$ is the fluid volume. Volume change $\Delta V$ can be written in terms of the piston displacements $x_{\text{L}}$ and $x_{\text{p}}$, the corresponding piston cross-sectional areas $A_{\text{L}}$ and $A_{\text{p}}$, and the volumetric displacement of the fluid chamber components. Expressing the latter in terms of the change in chamber pressure $\Delta p$ and the stiffness $C_o$ of the fluid chamber components, one gets

$$\Delta V = A_{\text{p}} x_{\text{p}} - A_{\text{L}} x_{\text{L}} - \frac{\Delta p}{C_o}. \tag{20}$$

Combination of (19) and (20) gives

$$\Delta p = \underbrace{\left( \frac{C_o \beta}{C_o V_{\text{ref}} + \beta} \right)}_{\beta_{\text{eff}}} \left( A_{\text{p}} x_{\text{p}} - A_{\text{L}} x_{\text{L}} \right). \tag{21}$$

Parameter $\beta_{\text{eff}}$ is an effective modulus which quantifies the compliance of the fluid and different fluid chamber components including the o-rings, pistons, and casing. The fundamental deformation equation which must be satisfied by the magnetostrictive rod at all times is

$$\lambda_{\text{avg}} - \frac{\sigma_{\text{c}}}{E} = \epsilon = \frac{x_{\text{p}} - x_{\text{s}}}{l_{\text{a}}}, \tag{22}$$

in which $\sigma_{\text{c}}$ is the compressive stress acting on the Terfenol-D rod of modulus $E$ and $l_{\text{a}}$ is the length of Terfenol-D rod. The force generated by the Terfenol-D, which has cross-sectional area $A_{\text{r}}$, is

$$F_{\text{a}} = \sigma_{\text{c}} A_{\text{r}} = E A_{\text{r}} \lambda_{\text{avg}} - \frac{E A_{\text{r}}}{l_{\text{a}}} (x_{\text{p}} - x_{\text{s}}). \tag{23}$$

The equations of motion for the two pistons and the support structure are

$$M_{\text{p}} \ddot{x}_{\text{p}} + (k_{\text{disk}})\, x_{\text{p}} + f r_{\text{p}} = -\Delta p A_{\text{p}} - \sigma_{\text{c}} A_{\text{r}}, \tag{24}$$

$$M_{\text{L}} \ddot{x}_{\text{L}} + (k_{\text{L}} + k_{\text{pre}}) x_{\text{L}} + f r_{\text{L}} = \Delta p A_{\text{L}}, \tag{25}$$

$$M_{\text{s}} \ddot{x}_{\text{s}} + k_{\text{s}} x_{\text{s}} = -F_{\text{a}}. \tag{26}$$

Parameters $k_{\text{L}}$ and $k_{\text{pre}}$ are the stiffness of the load and preload springs acting on the driven piston; $k_{\text{disk}}$ is the stiffness of the disk spring acting on the Terfenol-D rod; $f r_{\text{L}}$ and $f r_{\text{p}}$ denote the friction forces at the small and large piston, respectively. Friction at the smaller piston seal has a significant impact on the dynamic response of the actuator since actuation forces are low and velocities are high at this end. Actuation forces at the larger piston are high, hence a small frictional force would not have much effect on the dynamic response of the transducer. For this reason, it is essential to accurately quantify the friction dynamics at the smaller piston. The LuGre model for lubricated contacts [15] is used to model the frictional force based on the bristle interpretation of friction. The LuGre model equations are given by

$$\begin{aligned} \frac{\mathrm{d}z}{\mathrm{d}t} &= v - \sigma_0 \frac{|v|}{g(v)} z, \\ g(v) &= F_{\text{c}} + (F_{\text{s}} - F_{\text{c}}) \mathrm{e}^{-(v/v_{\text{s}})^2}, \\ F_{\text{r}} &= \sigma_0 z + \sigma_1(v) \frac{\mathrm{d}z}{\mathrm{d}t} + \sigma_2 v. \end{aligned} \tag{27}$$

Here, $z$ is the bristle deflection state, $F_{\text{s}}$ and $F_{\text{c}}$ are the static and Coulomb frictional forces, parameters $\sigma_0$, $\sigma_1$, $\sigma_2$ respectively denote the bristle stiffness, bristle damping and viscous damping coefficients, and $v_{\text{s}}$ is the Stribeck velocity. The Jiles–Atherton model parameters are listed in table 1; the LuGre model parameters are provided in table 2.

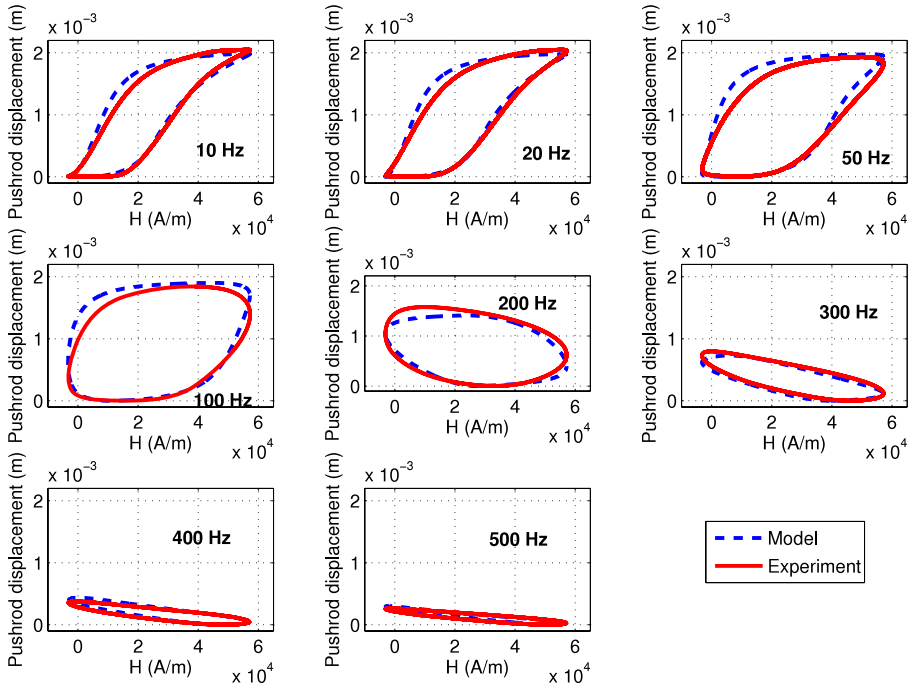


**Figure 5.** Output pushrod displacement at different actuation frequencies.

**Table 1.** Jiles–Atherton parameter values.

| Parameter | Value |
|---|---|
| $E$ (GPa) | 32 |
| $a$ (A m$^{-1}$) | 6512 |
| $c$ | 0.18 |
| $\alpha$ | 0.046 |
| $k$ (A m$^{-1}$) | 3000 |
| $\lambda_s$ | 1150 |
| $\sigma_{bias}$ (ksi) | −1.0 |
| $M_s$ (A m$^{-1}$) | $7.65 \times 10^5$ |

**Table 2.** Parameter values for the friction model.

| Parameter | Driven Piston (small) | Driver Piston (large) |
|---|---|---|
| $\sigma_0$ (N m$^{-1}$) | $0.34 \times 10^5$ | $1 \times 10^7$ |
| $\sigma_1$ (N s m$^{-1}$) | 35 | 0 |
| $\sigma_2$ (N s m$^{-1}$) | 4.3 | $5 \times 10^4$ |
| $v_s$ (m s$^{-1}$) | 0.0009 | 0.0009 |
| $F_c$ (N) | 5.2 (for $v > 0$) | 100 |
| | 11.0 (for $v < 0$) | |
| $F_s$ (N) | 5.8 (for $v > 0$) | 120 |
| | 11.1 (for $v < 0$) | |

## 5. Model results

The actuator was operated at discrete frequencies from 10 to 500 Hz with a total mechanical prestress of ≈1 ksi on the rod generated by the preload spring in contact with the driven piston. The preload spring also acts as the load spring as no external loading spring is attached to the pushrod. The Terfenol-D rod is magnetically biased with a field of ≈27 kA m$^{-1}$ by an Alnico magnet. The actuator is driven with a 4.5 A sinusoidal current with no current bias. The strain on the surface of the Terfenol-D rod is measured with a strain gage and the displacement of the pushrod is measured with a laser displacement sensor.

Figures 5 and 6 show the experimental and calculated time domain responses of the pushrod displacement and Terfenol-D strain at varied actuation frequencies. The model describes the hysteretic and nonlinear shape of the response both in terms of amplitude and phase. In the strain–field loops the modeled curves gradually become slightly more hysteretic than the experimental curves at higher frequencies. This could be because the model describes the average dynamic strain in the material while the strain gages measure the strain on the surface of the rod. At the surface the effect of diffusion would be absent while the average dynamic strain would increasingly lag behind the surface strain with increasing actuation frequency due to magnetic field diffusion, thereby leading to an increase in hysteresis.

A Fourier analysis on the experimental and calculated responses was conducted as shown in figures 7 and 8. The model accurately describes trends in the spectral content of the strain and displacement. Figures 9 and 10 show the magnitude and phase of the first-order component of the pushrod displacement and Terfenol-D strain, respectively. Strong correlation is obtained in the pushrod displacement response in both magnitude and phase. In the case of strain the magnitude matches well but there is some error in the phase at the higher frequencies. The cause for this inaccuracy in the phase description is the same as that for the increased hysteresis in the strain–field loops explained earlier. However, in almost all displacement amplified devices the primary concern is to predict the final output of the device accurately rather than the intermediate variables. In this case the output is the pushrod displacement which the model accurately quantifies over the entire frequency range.

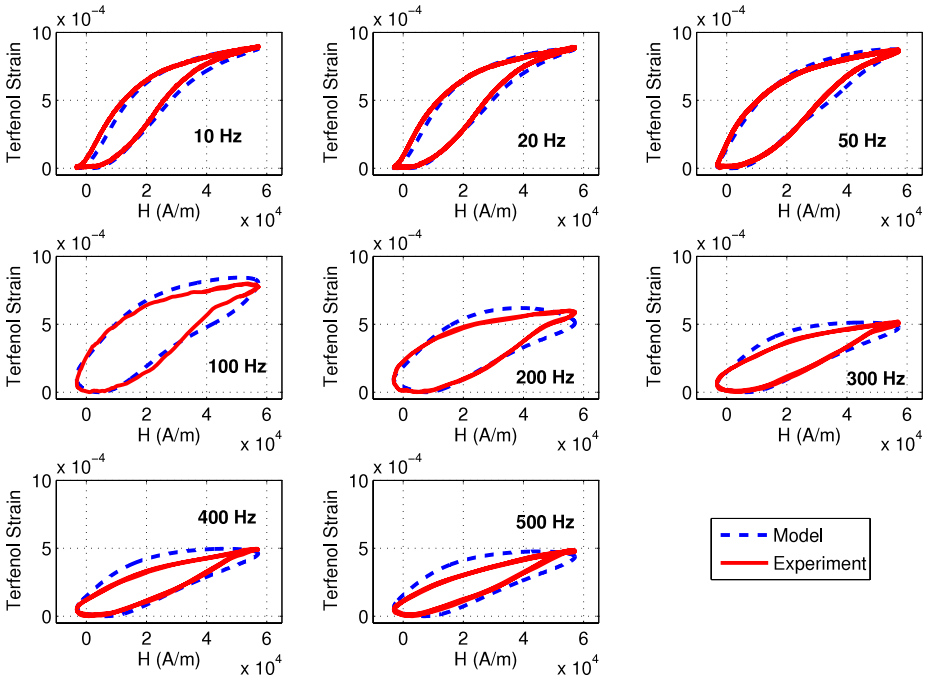


**Figure 6.** Terfenol-D strain at different actuation frequencies.

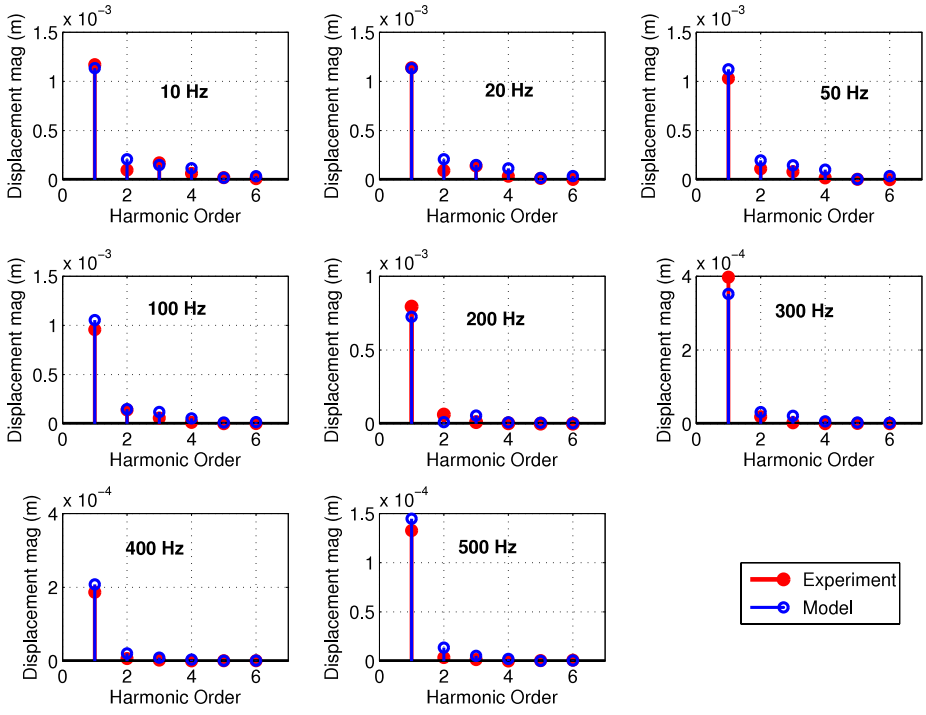


**Figure 7.** Output pushrod displacement orders.

## 6. Concluding remarks

A nonlinear model is presented which describes the dynamic response of a displacement amplified magnetostrictive actuator. Eddy current losses are modeled using Maxwell's equations. This gives rise to a radially dependent field in the magnetostrictive rod. The Jiles–Atherton model is used to quantify the magnetization in the rod as a function of the radially dependent field. Magnetostriction, calculated as a single-valued function of the magnetization, is averaged over the cross-section of the rod to obtain an effective magnetostriction. It is observed that this average magnetostriction becomes smaller in magnitude and increasingly lags behind the surface magnetostriction with an increase in drive frequency. The magnetic model is combined with the mechanical model describing the system vibrations. The LuGre friction model

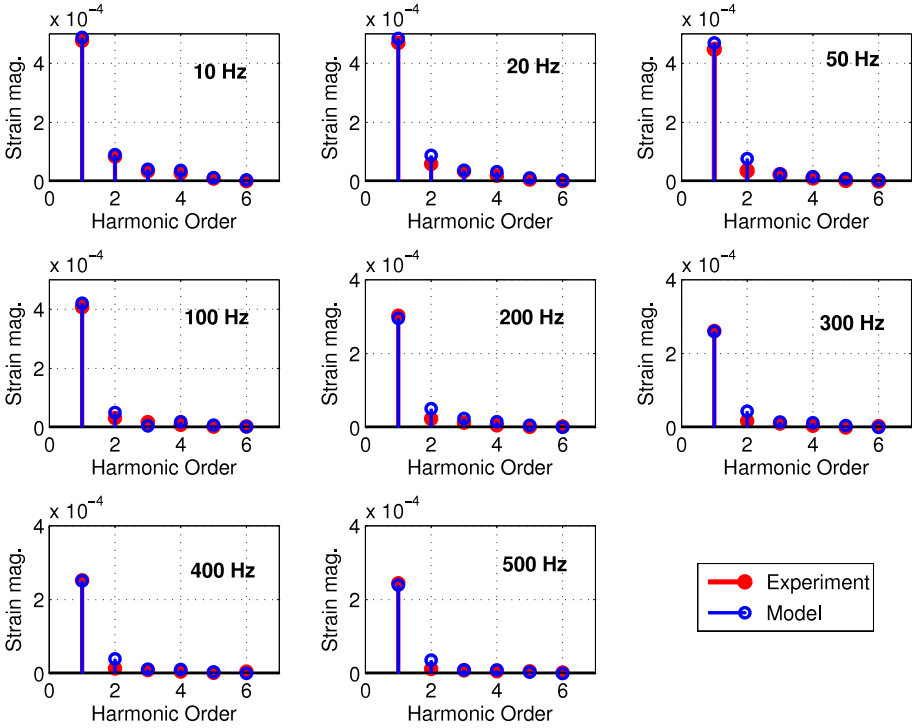


**Figure 8.** Terfenol-D strain orders.

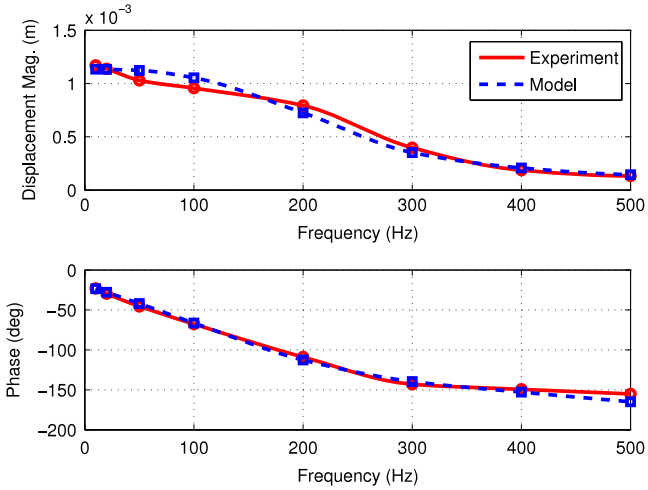


**Figure 9.** Output pushrod displacement magnitude and phase (first order).

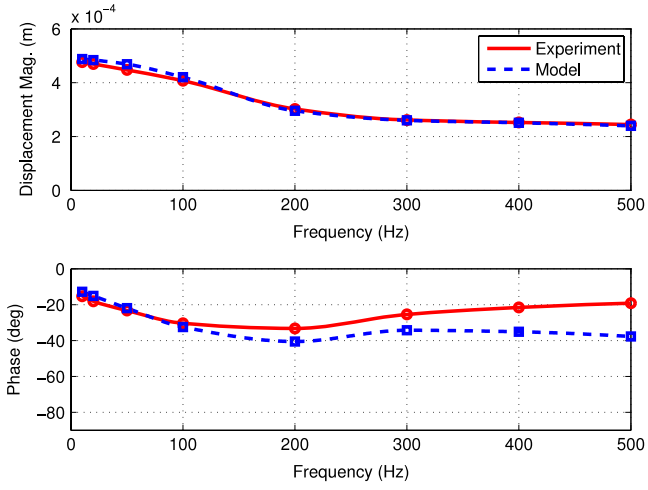


**Figure 10.** Terfenol-D strain magnitude and phase (first order).

is used to describe the frictional force at the output pushrod seal. It is observed that the LuGre model can describe the low velocity behavior of the device. The complete model describes the displacement-field and strain-field loops accurately up to 500 Hz. The nonlinearities in the response are also described with sufficient accuracy in terms of the higher-order spectral components, which are important for device control. At higher frequencies there are some inaccuracies in the strain–field loops due to the limitations of the constitutive model, friction model and unmodeled structural and fluid dynamics in the actuator.

## Acknowledgments

Financial support for this work was provided by the member organizations of the Smart Vehicle Concepts Center (www.SmartVehicleCenter.org), the National Science Foundation Industry/University Cooperative Research Centers Program, and the Smart Vehicle Concepts Center Fellowship Program.

## References

[1] Lee Y W and Lee C W 2002 Dynamic analysis and control of an active engine mount system *Proc. Instn. Mech. Eng.* D **216** 921–31

[2] Gennesseaux A 1995 A new generation of engine mounts *SAE* 951296
[3] Matsuoka H, Mikasa T and Nemoto H 2004 Nv countermeasure technology for a cylinder-on-demand engine—development of active control engine mount *SAE* 2004-01-0413
[4] Ushijima T and Kumakawa S 1993 Active engine mount with piezo-actuator for vibration control *SAE* 930201
[5] Shibayama T, Ito K, Gami T, Oku T, Nakajima Z and Ichikawa A 1995 Active engine mount for a large amplitude of engine vibration *SAE* 951298
[6] Nguyen V, Choi S, Han Y, Choi S and Moon S 2008 The design of a piezostack-based active mount and application to a vibration control system *Smart Mater. Struct.* **17** 065029
[7] Yoon H, Washington G, Eyabi P, Radhamohan M, Woodard S W and Dayton R 2006 A millimeter-stroke piezoelectric hybrid actuator using hydraulic displacement amplification mechanism *IEEE Int. Symp. Indust. Electron.* **4** 2809–13
[8] Giurgiutiu V, Rogers C A and Rusovici R 1996 Solid-state actuation of rotor blade servo-flap for active vibration control *J. Intell. Mater. Syst. Struct.* **7** 192–202
[9] Garcia-Bonito J, Brennan M J, Elliott S J, David A and Pinnington R J 1998 A novel high-displacement piezoelectric actuator for active vibration control *Smart Mater. Struct.* **7** 31–42
[10] Chakrabarti S and Dapino M J 2009 Design and modeling of a hydraulically amplified magnetostrictive actuator for automotive engine mounts *Proc. SPIE* **7290** 72900D
[11] Sarawate N N and Dapino M J 2008 A dynamic actuation model for magnetostrictive materials *Smart Mater. Struct.* **17** 065013
[12] Knoepfel H E 2000 *Magnetic Fields: a Comprehensive Theoretical Treatise for Practical Use* (New York: Wiley)
[13] Jiles D C and Atherton D L 1986 Theory of ferromagnetic hysteresis *J. Magn. Magn. Mater.* **61** 48–60
[14] Dapino M J, Smith R C, Calkins F T and Flatau A B 2002 A coupled magnetomechanical model for magnetostrictive transducers and its application to villari-effect sensors *J. Intell. Mater. Syst. Struct.* **13** 737–48
[15] Olsson H, Astrom K J, de Wit C C, Gafvert M and Lischinsky P 1998 Friction models and friction compensation *Eur. J. Control* **4** 176–95